



HHS Public Access

Author manuscript

Comput Methods Biomech Biomed Eng Imaging Vis. Author manuscript; available in PMC
2020 January 01.

Published in final edited form as:

Comput Methods Biomech Biomed Eng Imaging Vis. 2019 ; 7(4): 438–449. doi:
10.1080/21681163.2018.1523750.

A statistical framework for quantification and visualisation of positional uncertainty in deep brain stimulation electrodes

Tushar M Athawale^a, Kara A Johnson^a, Christopher R Butson^b, and Chris R Johnson^a

^aScientific Computing & Imaging (SCI) Institute, University of Utah, Salt Lake City, USA;

^bDepartment of Biomedical Engineering, University of Utah, Salt Lake City, USA

Abstract

Deep brain stimulation (DBS) is an established therapy for treating patients with movement disorders such as Parkinson's disease. Patient-specific computational modelling and visualisation have been shown to play a key role in surgical and therapeutic decisions for DBS. The computational models use brain imaging, such as magnetic resonance (MR) and computed tomography (CT), to determine the DBS electrode positions within the patient's head. The finite resolution of brain imaging, however, introduces uncertainty in electrode positions. The DBS stimulation settings for optimal patient response are sensitive to the relative positioning of DBS electrodes to a specific neural substrate (white/grey matter). In our contribution, we study positional uncertainty in the DBS electrodes for imaging with finite resolution. In a three-step approach, we first derive a closed-form mathematical model characterising the geometry of the DBS electrodes. Second, we devise a statistical framework for quantifying the uncertainty in the positional attributes of the DBS electrodes, namely the direction of longitudinal axis and the contact-centre positions at subvoxel levels. The statistical framework leverages the analytical model derived in step one and a Bayesian probabilistic model for uncertainty quantification. Finally, the uncertainty in contact-centre positions is interactively visualised through volume rendering and isosurfacing techniques. We demonstrate the efficacy of our contribution through experiments on synthetic and real datasets. We show that the spatial variations in true electrode positions are significant for finite resolution imaging, and interactive visualisation can be instrumental in exploring probabilistic positional variations in the DBS lead.

Keywords

Uncertainty visualisation; probabilistic computation; electrodes

1 Introduction

Biomedical imaging has become an integral part of clinical applications for analysing patient-specific anatomical structures. Imaging is processed through complex visualisation

CONTACT Tushar M Athawale tushar.athawale@sci.utah.edu Scientific Computing & Imaging (SCI) Institute, University of Utah, 72 Central Campus Dr, Salt Lake City 84112, USA.

Disclosure statement

No potential conflict of interest was reported by the authors.

models for making data more comprehensible. The quality of input images has a direct impact on the final visualisation, and hence, clinical decisions. In the domain of deep brain stimulation (DBS), Saleh et al. (2016) studied several imaging modalities, such as ultrasound imaging, intra-operative X-ray, intra-operative 3D X-ray, Medtronic O-arm, intra-operative MRI, and CT. In their work, computed tomography (CT) has been shown to be the safest and most accurate imaging technique to date in post-operative DBS.

Uncertainty is inherent to magnetic resonance (MR) and CT images because of the resolution limits that are dictated by the scanner, the length of time that the patient can remain still in the scanner (for MR), and the allowable radiation dose (for CT). Hence, most clinical imaging is a trade-off between acquisition time and resolution. Finite-resolution imaging can result in uncertainty in DBS electrode positions, but the uncertainty has never been quantified in a rigorous way. In our work, we address the issue of quantification and visualisation of uncertainty in DBS electrode positions arising from finite image resolution in Parkinsonian subjects.

DBS is a neuromodulation therapy that has shown promise in treating patients with intractable Parkinson's disease (PD). An electric field is applied to neural structures by implanting the DBS lead in the patient's brain. The neural response to the stimulation is highly sensitive to the electrode location and the stimulation settings (voltage, pulse width, and frequency) for the electrode contacts (Butson et al. 2007). Figure 2(a) depicts a schematic for the Medtronic 3387 human DBS lead with the four electrodes/contacts, as shown in Chaturvedi et al. (2010); Schmidt et al. (2012). The spatial extent of neural activation, otherwise known as the volume of tissue activated (VTA) (Butson et al. 2007), depends on the position of the contacts, the stimulation protocol, and the surrounding tissue structure. VTA influences the patient response to DBS.

DBS computational models of varying complexities play a key role in real-time estimation of VTA, and hence, the exploration of DBS stimulation effects (Chaturvedi et al. Gunalan et al. (2018) compared the state-of-the-art computational models for studying DBS stimulation effects. Specifically, the comparisons included the field-cable (FC), driving force (DF), and VTA models. The FC and DF models were shown to have lower computational errors but higher computational complexity than the VTA models. Clinical decision-making is so far not only dependent on modelling approaches but also can be enhanced, especially with the introduction of directional electrodes. Directional electrodes facilitate more control over VTA through novel electrode designs, such as segmented and multi-contact electrodes (Steigerwald et al. 2016). Reinacher et al. (2017) advocated 3D rotational fluoroscopy for determining the directions of electrode segments in implanted DBS leads.

Figure 1 depicts the patient-specific DBS modelling pipeline (Butson et al. 2007). Brain imaging for PD patients plays a vital role in pre-surgical and post-surgical decisions for DBS modelling. Initially, pre-operative MRI volumes are used for surgical planning prior to implantation of the DBS lead. The surgical plan specifies an entry point, trajectory, and depth of the lead for each individual patient. However, several factors during electrode implantation introduce uncertainty in frame-based stereotactic coordinates of the position of the DBS electrode relative to pre-operative imaging (Halpern et al. 2008; Khan et al. 2008).

The actual electrode positions are usually studied through acquisition of a post-operative CT scan. The post-operative CT/MR image is registered with a pre-operative MR image to study the positions of the DBS electrodes with respect to brain nuclei. Furthermore, the registered CT and MR images can be instrumental in quantifying differences between the planned and the actual electrode trajectory. The positions of the DBS lead contacts, the surrounding tissue structure, the proximity of neural nuclei, and the application of electric field are key to accurate quantification of stimulation effects using FC/DF/VTA models.

Post-operative imaging with finite resolution, however, limits our ability to identify exact electrode coordinates. The limited information about electrode coordinates often defeats the purpose of post-operative imaging since post-operative acquisitions are used to quantify the deviation of actual electrode positions from the planned positions in pre-operative imaging space. Moreover, the uncertainty in electrode positions diminishes our knowledge regarding nearby tissue structures. The material properties of the brain tissue surrounding the DBS electrodes play a critical role in estimating the spatial extent of neuron activation. Butson et al. (2006) showed that the electrode impedance has a substantial effect on the VTA, in which the electrode impedance is determined by several parameters, such as conductivity of the brain tissue and the encapsulation layer around the electrode contact. Schmidt et al. (2012) studied probabilistic variations in VTA caused by uncertainty in conductivity and permittivity of the brain tissue surrounding DBS electrodes. Thus, the lack of knowledge about nearby structures expands the DBS stimulation settings search space for getting optimal patient response, thereby making exploration of optimal stimulation settings time consuming.

In this paper, we propose a statistical model for characterising uncertainties in DBS electrode positions based on imaging resolution. The model takes into account electrode trajectory and inter-slice distance for a post-operative CT scan to compute the probabilistic spread of DBS electrodes. The visualisation of probabilistic variations in electrode positions gives insight into contact spread in physical space (millimetres) at different confidence levels. Additionally, the visualisation with respect to neural structures can be helpful in understanding the probabilistic overlap of the DBS electrodes with neural structures.

The problem of accurate DBS electrode localisation from post-operative DBS CT imaging is an active research field because of its significance in clinical decisions. Using correlated tri-planar displays for axial, sagittal, and coronal views is a standard way for gaining insight into DBS electrode positions. Hemm, Coste and Gabrillargues et al. (2009) deduced DBS electrode positions from the limits of lateral black artefacts in post-operative CT, the size of contacts and the inter-contact distance. Horn and Kuhn (2015) proposed a linear DBS electrode reconstruction model (*TRAC*) for reconstruction of an electrode trajectory. *TRAC* performs online processing of centroids of contact artefacts on axial slices in synergy with a linear regression model. In the contact reconstruction tool (*CORE*), a post-operative DBS CT scan is resampled parallel and orthogonal to the estimated lead trajectory for reconstructing the lead contact positions. For a linear electrode assumption, we propose a strategy for quantifying positional uncertainty in electrode reconstruction in contrast to approaches for a single electrode reconstruction (Sections 3.2 and 3.3). Husch et al. (2017) recently expanded linear DBS electrode models to take into account more realistic curved

models by employing curve-fitting algorithms. In the DBS surgery, the electrocorticography (ECoG) electrodes offer an opportunity to record cortical activity. Randazzo et al. (2016) proposed an ECoG electrode localisation strategy to recover missing depth information regarding electrodes in their fluoroscopic imaging.

The visualisation of DBS electrode reconstruction gives insight into the most probable electrode position, but keeps the end user oblivious to information about positional variations in the reconstructed DBS position. In our work, we address the challenge of visualisation of positional uncertainty in the DBS electrode. Confidence in positional error in the DBS electrode target resulting from the stereotactic process is crucial to neurosurgeons (Maciunas et al. 1994). Broadly speaking, the quantification and visualisation of uncertainty has become an important research challenge across all disciplines (Johnson and Sanderson 2003; Johnson 2004; Spiegelhalter et al. 2011). The uncertainties in a visualisation are attributed to algorithmic or hardware limitations as data is churned through several stages of the visualisation pipeline, such as the finite number of quantisation levels for data acquisition, the amplitude of data noise, the choice of computational model, and the rendering method (Pang et al. 1997; Brodlie et al. 2012). We study positional errors in DBS electrodes arising from a finite number of quantisation levels in the data acquisition phase.

Empirical evidence and statistical models are fundamental to quantifying algorithmic and data uncertainty. Maciunas et al. (1994) empirically derived the error in the electrode target arising from uncertain parameters relevant to the mechanics of the stereotactic process to be 2.28 mm with 99.9% confidence. In the context of visualisation, noise in data is often characterised by parametric and nonparametric statistical models to understand positional variations in level sets and direct volume rendering (Pöthkow et al. 2011; Athawale and Entezari, 2013; Pöthkow and Hege 2013; Athawale et al. 2015; Sakhaee and Entezari 2016; Hazarika et al. 2017; Athawale and Johnson 2019). In our work, we propose a statistical framework for predicting uncertainty in the parameters of DBS electrode reconstruction, specifically electrode trajectory and contact-centre positions. We apply a Bayesian statistical model to estimate the parameter distribution and integrate parameter uncertainty into visualisation.

Bayesian statistics plays an important role in decision support systems for medical diagnosis (Zuk 2008). A decision support system relies on observational evidence. The complex parameter space can lead to several possibilities and therefore reduce the cognitive transparency of an optimal decision. Visualisation of a posteriori probability can allow physicians to make quick and effective decisions. Vanlier et al. (2012) visualised the a posteriori probability of parameters of biochemical networks by combining colour maps with distribution plots. In the context of image processing, the inverse problem of image restoration from noisy or incomplete data is generally ill posed. The Bayesian paradigm plays a key role in the restoration of noisy and low-resolution images (Liu 2011). We quantify positional variations in DBS lead contacts by applying a Bayesian statistical model to a post-operative DBS CT scan. The uncertainties in electrode positions are visualised for efficient interpretation of the derived statistics.

A considerable body of literature addresses the challenge of visualising uncertainty in data (Pang et al. 1997; Bonneau et al. 2014). Colour mapping (Rhodes et al. 2003), point displacement (Grigoryan and Rheingans 2002, 2004), contour boxplots (Whitaker et al. 2013) and surface boxplots (Genton et al. 2014) are a few of the techniques for exploring uncertainty in complex datasets. In the point displacement technique, points on an isosurface are moved in a normal direction to indicate spatial variations in an isosurface. The contour boxplots and surface boxplots techniques identify representative isosurfaces for uncertain data by taking advantage of the concept of functional data depth (López-Pintado and Romo 2009). For example, the median isosurface has the highest functional data depth, and therefore, denotes the most likely isosurface for uncertain data. Quartiles of the data depth denote uncertainty in the median isosurface. In the context of DBS electrode reconstruction, Husch et al. (2017) visualised positional variations in DBS electrode reconstruction with boxplots. In the presented work, we interactively visualise positional uncertainty in DBS contacts through volume rendering and isosurfacing a probability density volume that characterises spatial variations in the DBS lead. The volume of spatial probability distribution is derived through a Bayesian statistical model.

2 Problem description

The finite resolution of post-operative CT imaging limits our understanding of true DBS electrode positions. Figure 2 illustrates the problem of positional uncertainty in DBS electrodes for CT imaging with finite resolution. In Figure 2(b), the red isosurface is reconstructed from a micro-CT scan of a Medtronic DBS electrode 3387 (Figure 2(a)) with the imaging resolution $0.033 \times 0.033 \times 0.033 \text{ mm}^3$. The high-resolution micro-CT volume is considered the gold standard. The horizontal slices superimposed on top of the red isosurface illustrate slices of a CT scan of DBS electrodes along the Z direction with an in-plane resolution of $0.5 \times 0.5 \text{ mm}^2$ and an inter-slice distance of 1mm.

We characterise the electrode positions with two parameters, the direction of the longitudinal axis for electrodes \mathbf{L} and the centres of cylindrical contacts $\mathbf{c} = \{c_0, c_1, c_2, c_3\}$, as shown in Figure 2(b). The proposed work assumes a linear DBS electrode model (Horn and Kuhn 2015), i.e. all contacts are assumed to be collinear. The CT image illustrated in Figure 2 (b) captures data on slices in the range 2–10 along the Z direction. For the illustration in Figure 2(b), the image of a single electrode is captured in voxels of at most two slices, thus missing substantial details about the underlying electrode positions. For example, the contact c_0 is captured on slices two and three. Thus, the accurate predictions regarding the trajectory and the position of the contact are difficult to make based on information acquired in only two slices. Moreover, data captured on slices is often blurred and noisy due to the partial volume effect (Kessler et al. 1984). Mathematically, the partial volume effect is a result of a low-pass filter, a point-spread function for scanner, and reconstruction noise (Marta and Szirmay-Kalos 2012). Maciunas et al. (1994) discuss the importance of fiducial geometry or the target being larger than the inter-voxel distance to avoid inaccuracies that might arise from subvoxel levels. In our work, we propose a framework for quantifying uncertainty in positional parameters, i.e. the direction of the longitudinal axis (\mathbf{L}) and the centre positions for contacts \mathbf{c} at subvoxel levels given sparse imaging data. Mathematically, we propose a framework for quantifying $Pr(\mathbf{c}, \mathbf{L}|I)$, where I denotes a postoperative DBS CT scan.

3 Methods

In this section, we present a three-step semi-automatic approach for quantifying positional uncertainty in DBS electrodes. First, we derive an analytical model for computing the physical limits of DBS electrodes given an electrode trajectory \mathbf{L} and an electrode geometry, e.g. contact length and intercontact distance (Section 3.1). Second, we propose an approach that leverages the analytical model derived in step one to quantify a solid angle representing directional uncertainty in longitudinal axis \mathbf{L} (Section 3.2). Last, we characterise positional uncertainties in the contact centres at subvoxel levels for the mean of the solid angle derived in step two (Section 3.3) and visualise uncertainties (Section 4).

3.1 Analytical model for computation of contact limits

In this section, we derive a mathematical model for computing the physical limits of Medtronic 3387 DBS lead contacts in the principal directions for basis $B = \{\mathbf{X}, \mathbf{Y}, \mathbf{Z}\}$. The schematic of the Medtronic 3387 DBS electrode geometry, which is similar to the ones presented in (Chaturvedi et al. 2010; Schmidt et al. 2012), is depicted in Figure 2(a), and the basis $B = \{\mathbf{X}, \mathbf{Y}, \mathbf{Z}\}$ is shown in Figure 3. The proposed model takes advantage of the electrode geometry and electrode direction to compute the physical limits of a contact. In Figure 3(a), the tilted cylinder represents contact c_0 . The centre of the contact c_0 is at the origin \mathbf{O} (not shown in Figure 3 to avoid clutter). We derive a new set of basis $N = \{\mathbf{L}, \mathbf{A}_1, \mathbf{A}_2\}$ along the electrode trajectory. The computation of basis N facilitates computation of the physical limits of lead contacts in basis B . The basis N is depicted in Figure 3(a). \mathbf{L} denotes the longitudinal axis of a cylindrical contact, \mathbf{A}_1 denotes the polar axis of a cylindrical contact, and \mathbf{A}_2 is orthogonal to \mathbf{L} and \mathbf{A}_1 .

Given \mathbf{L} points in a positive octant, we explain the construction of the polar axis \mathbf{A}_1 and a vector \mathbf{A}_2 . A similar construction mechanism is employed for electrode directions in other octants. In Figure 3(a), we derive spherical coordinates (a, b, c) for the principal vectors of basis N , where the quantities a , b , and c denote magnitude in millimetres, azimuth in degrees, and elevation in degrees, respectively. The spherical coordinates of \mathbf{L} are $(1.5/2; \theta, \phi)$, as depicted in Figure 3(a) and (b). The magnitude is set to the contact length along the electrode direction. We construct the polar axis \mathbf{A}_1 orthogonal to \mathbf{L} , where spherical coordinates for \mathbf{A}_1 are $(\frac{1.27}{2}; \theta + 180; 90 - \phi)$. The cross product of \mathbf{L} and \mathbf{A}_1 is evaluated to obtain \mathbf{A}_2 . The magnitudes of \mathbf{A}_1 and \mathbf{A}_2 are set to the length of the radius of cylinder, i.e. $\frac{1.27}{2}$ mm.

The physical limits of the DBS electrode contacts in the principal directions for basis $B = \{\mathbf{X}, \mathbf{Y}, \mathbf{Z}\}$ can be computed by marching along the principal directions for basis $N = \{\mathbf{L}, \mathbf{A}_1, \mathbf{A}_2\}$. For simplicity of discussion, we elaborate on a method for computing contact limits in the \mathbf{Y} direction. A similar approach is employed for computing contact limits in the other directions. Consider contact c_0 shown in Figure 3(a). Let \mathbf{A} represent a linear combination of \mathbf{A}_1 and \mathbf{A}_2 , which has a maximum physical stretch along the \mathbf{Y} direction. Let $a_1 Y$ and $a_2 Y$ denote \mathbf{Y} -components of vectors \mathbf{A}_1 and \mathbf{A}_2 , respectively. Let

$$\mathbf{A} = t_1 * \mathbf{A}_1 + t_2 * \mathbf{A}_2, \quad (1)$$

where t_1 and t_2 represent coefficients of mixing ($t_1 + t_2 = 1$). The Y-component of the vector \mathbf{A} , a_Y , can be rewritten as $t_1 * a_{1Y} + t_2 * a_{2Y}$. We search for the coefficient values t_1 and t_2 that maximise the absolute value of the Y-component of \mathbf{A} , i.e. $|a_Y|$ attains the maximum value by choosing the coefficient values of 1 and 0 for $\max(|a_{1Y}|, |a_{2Y}|)$ and $\min(|a_{1Y}|, |a_{2Y}|)$, respectively.

Depending upon the sign of a_{1Y} and a_{2Y} , the limits of contact c_0 in the \mathbf{Y} direction can be computed by marching along the principal directions for basis N . For example, if $|a_{1Y}| > |a_{2Y}|$, we find two new vectors, $\mathbf{a}_{y_{low}}$ and $\mathbf{a}_{y_{high}}$:

If $a_{1Y} > a_{2Y}$,

$$\mathbf{a}_{y_{low}} = \mathbf{O} - \mathbf{L} - \mathbf{A}_1 \quad (2)$$

$$\mathbf{a}_{y_{high}} = \mathbf{O} + \mathbf{L} + \mathbf{A}_1 \quad (3)$$

If $a_{1Y} < a_{2Y}$,

$$\mathbf{a}_{y_{low}} = \mathbf{O} - \mathbf{L} + \mathbf{A}_1 \quad (4)$$

$$\mathbf{a}_{y_{high}} = \mathbf{O} + \mathbf{L} - \mathbf{A}_1 \quad (5)$$

The Y-component of $\mathbf{a}_{y_{low}}$ represents the lowest point physical stretch, whereas the Y-component of $\mathbf{a}_{y_{high}}$ represents the highest point of physical stretch along the \mathbf{Y} direction for contact c_0 . A similar analysis is applied to find the physical limits of contact c_0 in the \mathbf{X} and \mathbf{Z} directions. The spatial limits of the remaining three contacts can be computed by adding multiples of $2 * \mathbf{L}$ to the physical limits for contact c_0 since the inter-contact distance is $2 * \mathbf{L}$ along the electrode trajectory, and contacts are assumed to be collinear.

3.2 Quantification of longitudinal uncertainty

We devise a technique for estimating a solid angle that represents longitudinal uncertainty in the DBS lead for post-operative imaging. The method exploits an analytical formulation proposed in Section 3.1 for quantifying longitudinal uncertainty. We describe our approach through an experiment on a synthetic dataset. First, we elaborate on parameters for generating synthetic datasets.

3.2.1 Parameter settings for creating synthetic datasets—A random vector corresponding to the longitudinal axis (**L**) direction is sampled with elevation $\theta \in [0, 45]$ and azimuth $\theta \in [0, 360]$. A high-resolution micro-CT scan of vertically oriented DBS electrodes is rotated along the sampled direction. The red isosurface shown in Figure 4 represents an isosurface reconstruction from a rotated micro-CT and is treated as the reference isosurface for direction **L**.

A rotated high-resolution micro-CT image is clipped to create a bounding box around the reference isosurface. The bounding box is padded with zeros along each dimension on both sides with a user's choice of thickness $[a * D_x, b * D_y, c * D_z]$ mm, where a, b, c are positive integers and $[D_x, D_y, D_z]$ denote the subsampling rate in millimetres. The resulting volume is down-sampled with an offset $[O_x, O_y, O_z]$, the sub-sampling rate $[D_x, D_y, D_z]$, and a Gaussian filter with a user's choice of support to create a test image. The Gaussian filter simulates the partial volume effect and a reconstruction noise in CT scans. The positions of the four contacts can be computed analytically in the high-resolution image space. For example, if c_y represents the physical stretch of a contact computed analytically (Section 3.1), the centre of contact c_0 is located at a distance of $b * D_y + \frac{c_y}{2}$ mm from the far left.

We illustrate our approach for creating a synthetic dataset in Figure 4, in which the bounding box around the isosurface is shown by the inner rectangle. The bounding box is padded with D_y and D_z millimetres along directions **Y** and **Z**. The padding is represented by the outer rectangle. The first dotted line from the left depicts the first slice taken along the **Y** direction at an offset O_y mm. The intensity value at the offset O_y is computed by centring a kernel of support D_y and performing a weighted average. The same process is repeated for computing the intensity values for successive slices. In Figure 4, the centre of the contact c_0 is located at a distance of $D_y + \frac{c_y}{2}$ from the far left along the **Y** direction.

3.2.2. An algorithm for quantifying longitudinal uncertainty—Algorithm 1 Trajectory Estimation

```

1: function MOSTPROBABLEDIRECTION( $[B_x, B_y, B_z]$ )
2:    $O \leftarrow$  an octant for direction of the electrode
3:    $n \leftarrow$  numberofMonteCarlo samples
4:    $o[1..n] \leftarrow$  uniformlysampledirectionsfromtheoctantO
5:   for  $i = 1$  to  $n$  do
6:      $[A_x, A_y, A_z] \leftarrow$  physical stretch of the four contacts computed analytically (Section 3.1)
7:      $dist[i] = \left\| [A_x, A_y, A_z] - [B_x, B_y, B_z] \right\|$ 
8:   end for
9:    $L \leftarrow o[\text{getindex}(\min(dist))]$ 
10:  return  $L$ 
11 end function

```

Having created a synthetic dataset, we propose a technique for estimating angular uncertainty in longitudinal axis **L**. First, we quantify the approximate physical stretch of the

four contacts from a synthetic image through observation. This is a manual step. For estimating an approximate physical stretch of the electrode, an isosurface is reconstructed from a synthetic dataset that represents the four blobs corresponding to the four contacts, as shown in Figure 5(a). We handpick two isovalues that represent the fattest isosurface and the thinnest isosurface for the four contacts. These isosurfaces allow us to estimate uncertainty in the physical boundaries for the four contacts in the X , Y , and Z directions by choosing two sets of imaging planes that contain these isosurfaces. For example, the red and the blue boundaries in Figure 5(a) denote inner and outer sets of imaging planes, respectively. The approximate physical stretch for isosurfaces is estimated through a number of imaging planes falling between boundary imaging planes and the inter-slice distance. For example, if nx is the number of imaging planes in the X direction within boundary imaging planes (red boundary in Figure 5(a)), then $B1_x = (nx - 1) * D_x$, where D_x is the inter-slice distance. Assuming that the minimum and maximum spatial spreads of the four contacts are $[B1_x, B1_y, B1_z]$ and $[B2_x, B2_y, B2_z]$, respectively, there are eight combinations of bounding boundaries representing uncertainty in the physical spread of the four contacts.

Next, we match the physical stretch of the four contacts, computed analytically (Section 3.1), with each of the eight bounding boundaries estimated from the image. Note that, in Section 3.1, we show a proof for computing the physical limits of a single contact. The same approach can be expanded to compute the physical limits of the four contacts in a given direction. Let $[B2_x, B1_y, B1_z]$ represent one of the eight bounding boundaries estimated from the image. The DBS lead trajectory for the electrodes is estimated by applying algorithm 5 to a bounding box $[B2_x, B1_y, B1_z]$. In the proposed algorithm, an octant containing the electrode trajectory is initially identified by applying a line fitting algorithm to centroids of the contact artefacts along the Z direction. This approach is similar to the TRAC tool proposed by Horn and Kuhn for trajectory reconstruction (Horn and Kuhn 2015).

The electrode trajectories are uniformly sampled from an octant in which the electrode resides. For each sampled direction, the physical stretch of the four contacts is computed analytically, and the analytical bounds are denoted by $[A_x, A_y, A_z]$. The direction with the minimum value of $\|[A_x, A_y, A_z] - [B2_x, B1_y, B1_z]\|$ is chosen as the most likely direction for the lead when the physical stretch of contacts is assumed to be $[B2_x, B1_y, B1_z]$. We get eight most likely direction estimates corresponding to eight sets of bounding image planes representing uncertainty in the physical stretch. For each direction, the spherical coordinates are computed. The grey patches shown in Figure 5(b) represent a solid angle evaluated by choosing minimum and maximum values of the azimuth and elevation among eight estimated directions. In Figure 5(b), the green line denotes the true DBS lead trajectory for the synthetic dataset, and it lies within the solid angle representing the longitudinal uncertainty in our experiments.

We validate our approach for uncertainty quantification in longitudinal axis L on 10 synthetic datasets. A synthetic dataset is generated for a trajectory randomly sampled from elevation $\phi \in [0, 45]$ degrees and azimuth $\theta \in [0, 360]$ degrees following the method described in Section 2.2.1. For each synthetic dataset, the offsets are sampled randomly, the subsampling rate is $0.45 \times 0.45 \times 1 \text{ mm}^3$, and a smoothing kernel is Gaussian with support $1 \times 1 \times 1 \text{ mm}^3$. The approximate physical limits are estimated for each dataset through

isosurfacing and estimating inner and outer bounding imaging planes representing uncertainty in the physical boundaries of the four electrodes. The variation is about one or two image planes on physical boundaries along each dimension in all datasets for the specified subsampling rate. Algorithm 5 is then run on each of the eight possible boundaries to estimate eight directions that carve a solid angle representing longitudinal uncertainty. In all 10 datasets, the true trajectory is contained within the solid angle, and the mean of uncertain directions lies within the angle of seven degrees from the true trajectories for the synthetic datasets. The mean trajectory is considered as the expected direction for DBS electrodes and is used for studying positional uncertainties at subvoxel levels in Section 3.3.

3.3 Quantification of positional uncertainties at subvoxel levels

Having computed longitudinal uncertainty, we characterise positional uncertainties in DBS electrodes at subvoxel levels and visualise them. Let $G(\mathbf{c}, \mathbf{L})$ represent the gold standard (high-resolution) image with contact-centre positions and contact direction specified by parameters \mathbf{c} and \mathbf{L} , respectively. According to Bayesian statistics, the posterior probability distribution is directly proportional to the product of the prior distribution (π) and the parameter likelihood (ψ). Mathematically,

$$Pr(\mathbf{c}, \mathbf{L}|I) \propto \pi(\mathbf{c}, \mathbf{L}) \cdot \psi(I; f(G(\mathbf{c}, \mathbf{L})))$$

We define the likelihood function ψ to be a comparison measure between the observed DBS imaging data (I) and a blurred version of the groundtruth image $f(G(\mathbf{c}, \mathbf{L}))$. In the groundtruth image, $G(\mathbf{c}, \mathbf{L})$, the contact positions are computed in closed form using the model described in Section 2.1. The blurring function f represents the subsampled version of the gold standard image $G(\mathbf{c}, \mathbf{L})$. The blurring function simulates the partial volume effect and reconstruction noise in real-world CT scans. The closer the blurred version of the groundtruth image $G(\mathbf{c}, \mathbf{L})$ to an observed image I , the higher is the likelihood associated with analytically computed parameters \mathbf{c} and \mathbf{L} for the groundtruth image.

Figure 6 summarises our approach for computing uncertainty in contact-centre positions at subvoxel levels. We now elaborate on each step shown in Figure 6. Let $\hat{\mathbf{L}}$ denote the mean of a solid angle representing longitudinal uncertainty (3.2.2). Initially, a micro-CT of DBS lead is oriented along the direction $\hat{\mathbf{L}}$ and is treated as the groundtruth image, $G(\mathbf{c}, \hat{\mathbf{L}})$. The likelihood values at subvoxel levels are estimated by Monte Carlo sampling the blurring function f and evaluating $\psi(I; f(G(\mathbf{c}, \hat{\mathbf{L}})))$. A Monte Carlo sample of the blurring function f is drawn by following the same process for creating synthetic datasets (Section 3.2.1). For example, Figure 4 illustrates a Monte Carlo sample at an offset O_y along the Y direction. In Figure 4, the first slice is taken at O_y mm, and all successive slices are taken at a multiple of subsampling rate D_y mm. Let c_y represent the physical stretch of contact along the Y direction computed analytically using the closed-form model described in 2.1. The centre of contact \mathbf{c}_0 is located at distance $D_y + \frac{c_y}{2} - O_y$ from the first slice. Thus, we model subvoxel positions by sampling offsets $[O_x, O_y, O_z]$ at a resolution higher than the subsampling rate $[D_x, D_y, D_z]$ for each Monte Carlo sample.

The Monte Carlo sample is compared with observed imaging data to estimate the likelihood $\psi(I; f(G(\mathbf{c}, \hat{\mathbf{L}})))$, and the likelihood value is assigned to a closed-form contact-centre position associated with a Monte Carlo sample. In our work, we utilise an image-gradient based approach to compute the likelihood function $\psi(I; f(G(\mathbf{c}, \hat{\mathbf{L}})))$. Specifically, for a CT scan of DBS electrode contacts, the image gradient is relatively high close to centres of cylindrical contacts, and the gradient recedes as we move away from contact centres along radial directions in the imaging space. The likelihood function $\psi(I; f(G(\mathbf{c}, \hat{\mathbf{L}})))$ is evaluated by computing the structural similarity index *SSIM* (Wang et al. 2004) between the gradient fields for images I and $f(G(\mathbf{c}, \hat{\mathbf{L}}))$:

$$\psi(I; f(G(\mathbf{c}, \hat{\mathbf{L}}))) = SSIM(\nabla I, \nabla f(G(\mathbf{c}, \hat{\mathbf{L}}))), \quad (6)$$

In the proposed framework, we do not assume any prior knowledge about contact-centre positions at subvoxel levels. Therefore, we model the prior density $\pi(\mathbf{c}, \hat{\mathbf{L}})$ with a uniform distribution. We, therefore, interpret the normalised likelihood function as a posterior probability distribution $\Pr(\mathbf{c}, \hat{\mathbf{L}}|I)$.

4 Results and discussion

We demonstrate the effectiveness of the presented methods through experiments on 2D and 3D synthetic datasets and the real dataset. All code for this project is implemented in MATLAB. The resulting images are visualised in ParaView (Ahrens et al. 2005). In the first experiment, the statistical framework for quantifying subvoxel level uncertainties (Section 3.3) is validated through results on a synthetically generated 2D Gaussian dataset. The results are visualised in Figure 7. The gradient for the Gaussian function is relatively high near its mean but falls off as we move away from the mean towards the boundaries. The groundtruth image for the experiment is created by sampling a 2D Gaussian field on a high-resolution grid with the mean $[0, 0]$, the variance of 5 mm^2 along each dimension, and the covariance of 0.3 mm^2 , as depicted in Figure 7(a) with the grey map. The groundtruth image is subsampled by following an approach for generating synthetic datasets (Section 3.2.1). The subsampling is performed starting at an offset position $[\mathbf{O}_x, \mathbf{O}_y] = [-10, -10] \text{ mm}$ and the subsampling rate $[0.5, 1] \text{ mm}$. The resulting image is visualised in Figure 7(b) and is treated as the test image. The width of the test image is half its height because of the subsampling rate. Having created the test image, we derive uncertainties at subvoxel positions for the test image using the statistical framework proposed in Section 3.3.

In the first step, Monte Carlo samples are drawn from the groundtruth image. Each Monte Carlo sample represents a subsampled version of the groundtruth image. As a pre-processing step for subsampling, the groundtruth image is padded with zeros along the X and Y directions for the length of $[10 * D_x, 10 * D_y] \text{ mm}$ on both sides. The padded image is shown in Figure 7(c). The Monte Carlo samples are drawn by sampling offset values $[\mathbf{O}_x, \mathbf{O}_y]$ in the range $[-10 - 3 * D_x, -10 + 3 * D_x] \text{ mm}$ and $[-10 - 3 * D_y, -10 + 3 * D_y] \text{ mm}$ at a finer resolution of $[0.1, 0.1] \text{ mm}$ in the padded groundtruth image space (Figure 7(c)). The results for the specified offset ranges are visualised in Figure 7(d, e, and f).

Each Monte Carlo sample is compared with the test image (Figure 7(b)) using Equation (6), and the likelihood estimate is assigned to the offset position associated with the sample. The *SSIM* index is anticipated to be relatively high for samples with the offset positions closer to $[O_x, O_y] = [-10, -10]$ mm. The results visualised in Figure 7(d, e, and f)) confirm what we had anticipated. The *SSIM* index is relatively high when offset $[O_x, O_y]$ is close to $[-10, -10]$ mm for all three images. The range of the sampled offsets for the results shown in Figure 7 (e) and in Figure 7(f) are the same as for the offset range shown in Figure 7(d). The drop in the *SSIM* values is sharp when contrast and structural similarity parameter values associated with the *SSIM* index are large.

We design the second experiment on a 3D synthetic dataset for visualisation of uncertainty in DBS electrode positions, as shown in Figure 8. First, a test dataset is generated for a random electrode trajectory, fixed offset values, the subsampling rate of $0.45 \times 0.45 \times 1$ mm³, and a Gaussian kernel of width $1 \times 1 \times 1$ mm³. The subsampling method described in Section is applied to a high-resolution micro-CT scan of DBS electrodes oriented along a sampled trajectory for creating the test image. Having created a test image, we quantify and visualise positional uncertainties in the DBS electrodes. First, a solid angle indicating longitudinal uncertainty in DBS electrodes is derived by applying the algorithm proposed in Section 3.2.2 to the synthetic dataset. The solid angle is represented in Figure 5(b). The mean of the solid angle is considered as the expected direction of the electrodes.

The positional uncertainties at subvoxel positions are derived for the test image (Section 3.3) assuming that the DBS electrodes are oriented along the mean of uncertain trajectories. First, a micro-CT of DBS electrodes is rotated along the mean of uncertain trajectories. The image is padded with a fixed number of zero planes on both sides. Monte Carlo samples representing uncertainty in the offsets are drawn by sampling the offsets at the subvoxel sampling rate of $0.2 \times 0.2 \times 0.2$ mm³ and a Gaussian kernel of width $1 \times 1 \times 1$ mm³. The *SSIM* index values are derived through image comparison between Monte Carlo samples and the test image using Equation (6). The *SSIM* values are assigned to analytically computed contact-centre positions associated with each Monte Carlo sample. Higher index values imply a higher likelihood for contact-centre positions and vice versa. We also record the true contact-centre positions for the test image.

The *SSIM* values for Monte Carlo samples representing subvoxel positions are visualised in Figure 8, in which the left column visualises volume rendering of relative *SSIM* values. In the transfer function for volume rendering, higher opacities are mapped to higher probability regions and vice versa. The spheres in all sub-images indicate the true contact-centre positions for the test image. In the middle and the right columns, isosurfaces are rendered for the relative likelihood values 0.9 and 0.95, respectively. The grey lines in the isosurface images depict the expected direction of electrodes. The volume and isosurface visualisations enable us to gain insight into the probabilistic spread of contact-centre positions.

Through interactive 3D visualisation, we verify that the true contact-centre positions reside close to those with relatively high probability. The interactive visualisation is presented through multiple views in Figure 8. Each row shows volume rendering and isosurfaces for a fixed view point and zoom-in levels. In all three viewpoints, spherical glyphs representing

true contact centres are close to regions of relatively high contact-centre likelihood/*SSIM* index, which proves the correctness of the approach for deriving positional uncertainties. The probability distribution over contact-centre positions allows us to compute the expected position and standard deviation from the expected position. The standard deviations for the isosurfaces with relative likelihood values 0.9 and 0.95 are 0.38mm and 0.28mm, respectively.

In the last experiment, Figure 9 visualises a result for the real dataset similar to one for the 3D synthetic dataset. We acquired access to the real dataset from the International Neuromodulation Registry at the University of Utah. The positional uncertainties in DBS electrode centres are studied for a post-operative CT scan of a bilaterally implanted DBS PD subject with an imaging resolution of $0.45 \times 0.45 \times 1 \text{ mm}^3$. Figure 9 visualises uncertainty in contact-centre positions at subvoxel levels for the same subject. Monte Carlo samples representing subvoxel positions are drawn by down-sampling a micro-CT rotated along the expected direction (3.2.2) with a subsampling rate $0.45 \times 0.45 \times 1 \text{ mm}^3$ and offset sampling of $0.2 \times 0.2 \times 0.2 \text{ mm}^3$. The groundtruth is smoothed with the Gaussian kernel of width $3 \times 3 \times 3 \text{ mm}^3$ before subsampling. The likelihood values are estimated by comparing Monte Carlo samples with observed data using Equation (6) and visualised in Figure 9. The empirically computed spatial standard deviations of isosurfaces for the relative likelihood values 0.9 and 0.95 from the mean centre position are 0.71 mm and 0.48 mm, respectively.

The proposed approach for computing spatial distribution of contact centres is sensitive to the choice of kernel, the kernel width, and the parameters of *SSIM* index, specifically, the exponent values for contrast and structure parameters. The choice of a kernel width smaller than the true kernel width can result in visualisation artefacts showing discontinuities in the probability distribution. For example, consider the result shown in Figure 10 demonstrating the sensitivity of spatial density estimates to the kernel width. The results are shown for the real dataset experiment in Figure 9. As the kernel support is increased from $2 \times 2 \times 2 \text{ mm}^3$ to $3 \times 3 \times 3 \text{ mm}^3$, the visualisation result gets smoother. Intuitively, the positional distribution for contact centres should be smoother and gradually decreasing as we move away from the most probable contact-centre positions. We observe relatively smooth behaviour in density estimates when the kernel width is $3 \times 3 \times 3 \text{ mm}^3$. In all sub-images of Figure 10, however, the regions of contact centres with relatively high probabilities are consistently recovered throughout.

Regarding the choice of contrast and structure parameters of the *SSIM* index, very high values of indices can result in overfitting of the probability estimation to local imaging details. However, small values of contrast and structure parameters can result in the overestimation of probabilities at spatial positions where contact centres have a low probability of existence. These two cases are evident from the results shown on a 2D synthetic dataset in Figure 7(d and f). Therefore, for all experiments, we choose contrast and structure parameter values as 5 and 5, respectively. A sample result for 2D synthetic dataset is shown in Figure 7(e).

5 Conclusion and future work

We study the problem of positional uncertainty in the DBS electrodes for post-operative CT imaging with finite resolution. We propose a framework for quantifying longitudinal and subvoxel level variations in DBS lead contacts by taking advantage of analytical characterisation of DBS lead geometry. The statistics representing positional variations can be efficiently interpreted through interactive visualisation techniques, such as volume rendering and isosurfaces. We show that the uncertainty in electrode positions is significant for finite-resolution imaging and should be incorporated into DBS computational models for accurate predictions of DBS effects.

In the future, we plan to propagate positional uncertainties in DBS electrodes into electric field simulation for studying variations in the VTA (Butson et al. 2007). We plan to incorporate quantification of lead positional uncertainty with the analysis of electrode impedance for estimating the extent of neuron activation (Butson et al. 2006; Schmidt et al. 2012), and hence, improving predictions of the effects of DBS in individual subjects. We also plan to derive positional uncertainties for curved electrode models (Husch et al. 2017).

Acknowledgments

Funding

This project is supported in part by the National Institute of General Medical Sciences of the National Institutes of Health (grant number P41 GM103545–18) and the University of Utah Neuroscience Initiative Neural Circuits grant.

References

- Ahrens J, Geveci B, Law C. 2005 ParaView: an end-user tool for large data visualization, chap. 36. Elsevier, p. 717–731. https://books.google.com/books?hl=en&lr=&id=mA8ih1AieaYC&oi=fnd&pg=PP1&ots=DJZbIwq9Eq&sig=P6Uc-PnJ5rck0Ryn_2U7D4fj5g8#v=onepage&q&f=false
- Athawale T, Entezari A. 2013 Oct. Uncertainty quantification in linear interpolation for isosurface extraction. *IEEE Trans Vis Comput Graph*. 19(12):2723–2732. doi:10.1109/TVCG.2013.208 [PubMed: 24051839]
- Athawale T, Johnson CR. 2019 Jan. Probabilistic asymptotic decider for topological ambiguity resolution in level-set extraction for uncertain 2d data. *IEEE Trans Visual Comput Graph*. 25(1):doi: 10.1109/TVCG.2018.2864505
- Athawale T, Sakhaee E, Entezari A. 2015 Aug. Isosurface visualization of data with nonparametric models for uncertainty. *IEEE Trans Vis Comput Graph*. 22(1):777–786. doi:10.1109/TVCG.2015.2467958
- Bonneau G, Hege H-C, Johnson CR, Oliveira M, Potter K, Rheingans P, Schultz T. 2014 Sept. Overview and state-of-the-art of uncertainty visualization In: Hansen C, Chen M, Johnson CR, Kauffman A, Hagen H, editors. *Scientific visualization, mathematics and visualization*. London: Springer; p. 3–27. doi:10.1007/978-1-4471-6497-5_1
- Brodie K, Allendes Osorio R, Lopes A. 2012 A review of uncertainty in data visualization. *Expand Frontiers Visual Anal Visual*. 81–109. doi:10.1007/978-1-4471-2804-5_6
- Butson CR, Cooper SE, Henderson JM, McIntyre CC. 2007 Jan. Patient-specific analysis of the volume of tissue activated during deep brain stimulation. *NeuroImage*. 34(2):661–670. doi:10.1016/j.neuroimage.2006.09.034 [PubMed: 17113789]
- Butson CR, Maks CB, McIntyre CC. 2006 Feb. Sources and effects of electrode impedance during deep brain stimulation. *Clin Neurophysiol*. 117(2):447–454. doi:10.1016/j.clinph.2005.10.007 [PubMed: 16376143]

- Chaturvedi A, Butson C, Lempka S, Cooper S, McIntyre C. 2010 April. Patient-specific models of deep brain stimulation: influence of field model complexity on neural activation predictions. *Brain Stimul.* 3 (2):65–67. doi:10.1016/j.brs.2010.01.003 [PubMed: 20607090]
- Follett KA, Weaver FM, Stern M, Hur K, Harris CL, Luo P, Marks WJJ, Rothlind J, Sagher O, Moy C, et al. 2010 June. Pallidal versus subthalamic deep-brain stimulation for parkinson's disease. *New Engl J Med.* 362(22):2077–2091. doi:10.1056/NEJMoa0907083 [PubMed: 20519680]
- Genton MG, Johnson CR, Potter K, Stenichikov G, Sun Y. 2014 Surface boxplots. *Stat J.* 3(1):1–11.
- Grigoryan G, Rheingans P. Probabilistic surfaces: point based primitives to show surface uncertainty In *IEEE Visualization '02*, pp.147–153. IEEE Press, Oct. 2002. doi: 10.1109/VISUAL.2002.1183769
- Grigoryan G, Rheingans P. 2004 July. Point-based probabilistic surfaces to show surface uncertainty. *IEEE Trans Vis Comput Graph.* 10(5):564–573. doi:10.1109/TVCG.2004.30 [PubMed: 15794138]
- Gunalan K, Howell B, McIntyre CC. 2018 Quantifying axonal responses in patient-specific models of subthalamic deep brain stimulation. *NeuroImage.* 172:263–277. doi:10.1016/j.neuroimage.2018.01.015 [PubMed: 29331449]
- Halpern C, Danish S, Baltuch G, Jaggi J. 2008 Brain shift during deep brain stimulation surgery for Parkinson's disease. *Steriotact Funct Neurosurg.* 86(1):37–43.
- Hazarika S, Biswas A, Shen H-W. 2017 Aug. Uncertainty visualization using copula-based analysis in mixed distribution models. *Trans Visual Comput Graph IEEE.* 24(1):934–943. doi:10.1109/TVCG.2017.2744099
- Hemm S, Coste J, Gabrillargues J, Ouchchane L, Sarry L, Caire F, Vassal F, Nuti C, Derost P, Durif F, et al. 2009 July. Contact position analysis of deep brain stimulation electrodes on post-operative CT images. *Acta Neurochir.* 151(7):823–829. doi:10.1007/s00701-009-0393-3 [PubMed: 19444372]
- Horn A, Kuhn AA. 2015 Lead-DBS: a toolbox for deep brain stimulation electrode localizations and visualizations. *NeuroImage.* 107:127–135. doi:10.1016/j.neuroimage.2014.12.002 [PubMed: 25498389]
- Husch A, Petersen MV, Gemmar P, Goncalves J, Hertel F. 2017 Pacer - a fully automated method for electrode trajectory and contact reconstruction in deep brain stimulation. *NeuroImage Clin.* 17:80–89. doi:10.1016/j.nicl.2017.10.004 [PubMed: 29062684]
- Johnson CR. 2004 Jul-Aug Top scientific visualization research problems. *IEEE Comput Graph Appl Visual Viewpoints.* 24(4):13–17. doi:10.1109/MCG.2004.20
- Johnson CR, Sanderson AR. 2003 Sep-Oct A next step: visualizing errors and uncertainty. *IEEE Comput Graph Appl.* 23(5):6–10. doi:10.1109/MCG.2003.1231171
- Kessler RM Jr, JRE, Eden M 1984 Analysis of emission tomographic scan data: limitations imposed by resolution and background. *J Comput Assist Tomogr.* 8(3):514–522. [PubMed: 6609942]
- Khan M, Mewes K, Gross R, Skrinjar O. 2008 Assessment of brain shift related to deep brain stimulation surgery. *Steriotact Funct Neurosurg.* 86(1):44–53.
- Liu Z-Q. 2011 Bayesian paradigms in image processing, Vol. 24 Singapore: World Scientific. doi: 10.1142/9789812797711_0002
- Lopez-Pintado S, Romo J. 2009 June. On the concept of depth for functional data. *J Am Stat Assoc.* 104(486):718–734. doi:10.1198/jasa.2009.0108
- Maciunas R, Galloway R, Latimer J. 1994 Oct. The application accuracy of stereotactic frames. *Neurosurgery.* 35(4):682–694. doi:10.1227/00006123-199410000-00015 [PubMed: 7808612]
- Marta Z, Szirmay-Kalos L. Partial volume effect correction using segmented CT images with distance mapping. In *Sixth Hungarian Conference on Computer Graphics and Geometry*, pp. 1–8, 2012.
- Pang A, Wittenbrink C, Lodha S. 1997 Nov. Approaches to uncertainty visualization. *Vis Comput.* 13(8):370–390. doi:10.1007/s003710050111
- Pothkow K, Hege H-C. 2013 July. Nonparametric models for uncertainty visualization. *Computer Graphics Forum.* 32(3.2):131–140. doi:10.1111/cgf.12100
- Pothkow K, Weber B, Hege H-C. 2011 June. Probabilistic marching cubes. *Computer Graphics Forum.* 30(3):931–940. doi:10.1111/j.1467-8659.2011.01942.x
- Randazzo MJ, Kondylis ED, Alhourani A, Wozny TA, Lipski WJ, Crammond DJ, Richardson RM. 2016 Three-dimensional localization of cortical electrodes in deep brain stimulation surgery for

- intraoperative fluoroscopy. *NeuroImage*. 125:515–521. doi:10.1016/j.neuroimage.2015.10.076 [PubMed: 26520771]
- Reinacher PC, Kruger MT, Coenen VA, Shah M, Roelz R, Jenkner C, Egger K. 2017 Jun. Determining the orientation of directional deep brain stimulation electrodes using 3d rotational fluoroscopy. *AJNR Am J NeuroRadiol*. 38(6):1111–1116. doi:10.3174/ajnr.A5153 [PubMed: 28385887]
- Rhodes PJ, Laramée RS, Bergeron RD, Sparr TM. Uncertainty visualization methods in isosurface rendering In *EUROGRAPHICS 2003 Short Papers*, pp. 83–88. Eurographics Association, 2003. doi: 10.2312/egs.20031054
- Sakhaee E, Entezari A. 2016 Dec. A statistical direct volume rendering framework for visualization of uncertain data. *IEEE Trans Vis Comput Graph*. 23(12):2509–2520. doi:10.1109/TVCG.2016.2637333 [PubMed: 27959812]
- Saleh C, Dooms G, Berthold C, Hertel F. 2016 Aug. Post-operative imaging in deep brain stimulation: a controversial issue. *Neuroradiol J*. 29 (4):244–249. doi:10.1177/1971400916639960 [PubMed: 27029393]
- Schmidt C, Grant P, Lowery M, Rienen UV. 2012 Dec. Influence of uncertainties in the material properties of brain tissue on the probabilistic volume of tissue activated. *IEEE Trans Biomed Eng*. 60(5):1378–1387. doi:10.1109/TBME.2012.2235835 [PubMed: 23269746]
- Spiegelhalter D, Pearson M, Short I. 2011 Sept. Visualizing uncertainty about the future. *Science*. 333(6048):1393–1400. doi:10.1126/science.1191181 [PubMed: 21903802]
- Steigerwald F, Müller L, Johannes S, Matthies C, Volkmann J. 2016 Aug. Directional deep brain stimulation of the subthalamic nucleus: a pilot study using novel neurostimulation device. *Mov Disord*. 31(8):1240–1243. doi:10.1002/mds.26669 [PubMed: 27241197]
- Vanlier J, Tiemann C, Hilbers P, van Riel N. 2012 Apr. An integrated strategy for prediction uncertainty analysis. *Bioinformatics*. 28 (8):1130–1135. doi:10.1093/bioinformatics/bts088 [PubMed: 22355081]
- Wang Z, Bovik A, Sheikh H, Simoncelli E. 2004 Apr. Image quality assessment: from error visibility to structural similarity. *IEEE Trans Image Process*. 13(4):600–612. doi:10.1109/TIP.2003.819861 [PubMed: 15376593]
- Whitaker R, Mirzargar M, Kirby R. 2013 Oct. Contour boxplots: a method for characterizing uncertainty in feature sets from simulation ensembles. *IEEE Trans Vis Comput Graph*. 19(12): 2713–2722. doi:10.1109/TVCG.2013.143 [PubMed: 24051838]
- Zuk TD. *Visualizing Uncertainty*. PhD thesis, University of Calgary, Calgary (Alta, Canada), 2008.

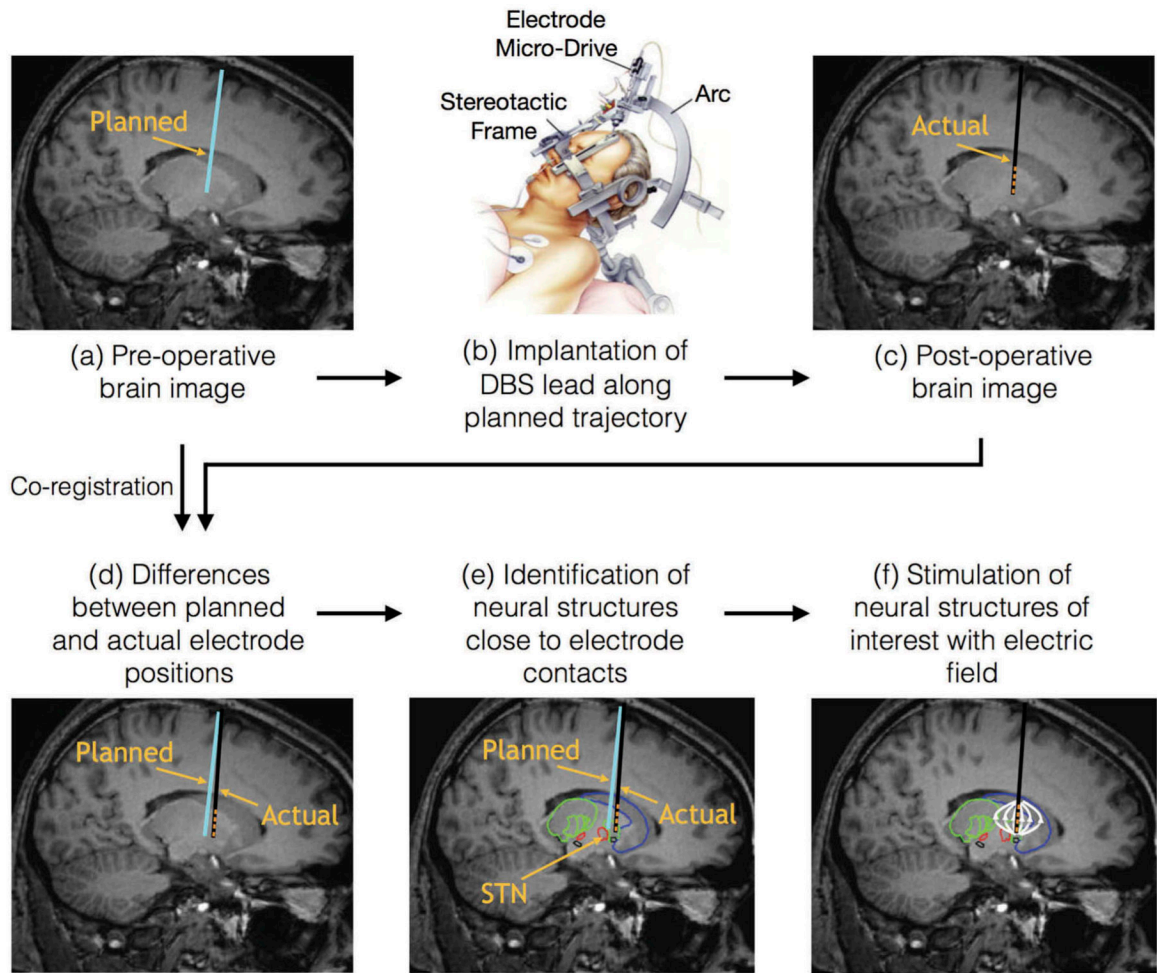


Figure 1.

The DBS modelling pipeline: (a) The DBS lead position in the patient brain is planned based on the tissue structures studied from pre-operative imaging. For example, the planned lead trajectory is depicted with a line coloured in cyan. (b) The DBS lead is implanted along the planned trajectory using a stereotactic frame. (c) The actual lead trajectory and the electrode positions in the patient brain are captured through post-operative imaging and are illustrated using a black line and four orange dots, respectively. (d) Co-registration of the post-operative imaging with the pre-operative imaging is instrumental in understanding differences in the planned and the actual electrode positions. (e) Several neural structures in the proximity of electrodes are illustrated with green, blue, and red boundaries. The sub-thalamic nucleus (STN), indicated by a red boundary, is the most common neural target for DBS (Follett et al. 2010). (f) The electrical field depicted with white arcs is modulated depending upon the proximity of neural structures of interest for predicting the optimal patient response.

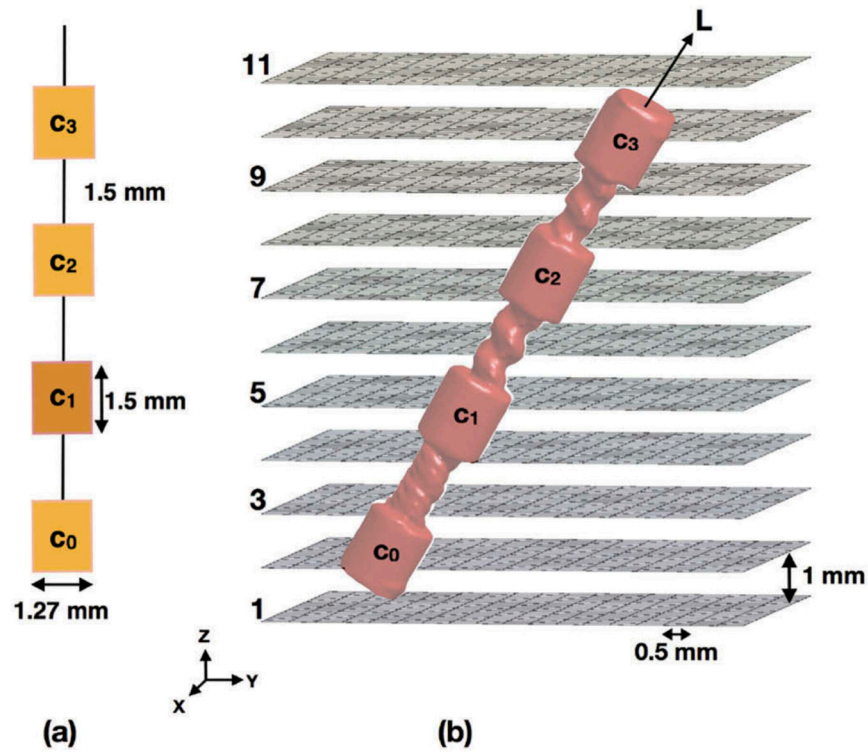


Figure 2.

Positional uncertainty in DBS electrodes for finite-resolution imaging: (a) A schematic for Medtronic 3387 DBS lead. The orange regions indicate the four cylindrical electrodes/contacts. The stimulation settings (voltage, frequency, pulse width) as well as the activation state for each of the contacts can be configured independently. For example, the contact c_1 is active and is depicted in dark orange. The contact diameter is 1.27 mm, the contact length is 1.5 mm and the inter-contact distance is 1.5 mm. (b) The red isosurface represents an isosurface reconstructed from a high-resolution image ($0.033 \times 0.033 \times 0.033 \text{ mm}^3$) of the Medtronic DBS electrode 3387 oriented along direction L . The 11 horizontal slices depict slices of a CT scan (a real-world scenario) of DBS electrodes with resolution $0.5 \times 0.5 \times 1 \text{ mm}^3$. The CT scan captures electrode positions on slices in the range 2–10. In this illustration, the image of a single electrode is captured in voxels of at most two slices, e.g. the contact c_0 is captured on slices two and three. The sparse data on slices of CT scan introduces uncertainty in the direction of the longitudinal axis L and in the positions of contact centres $\mathbf{c} = [c_0, c_1, c_2, c_3]$ at subvoxel levels.

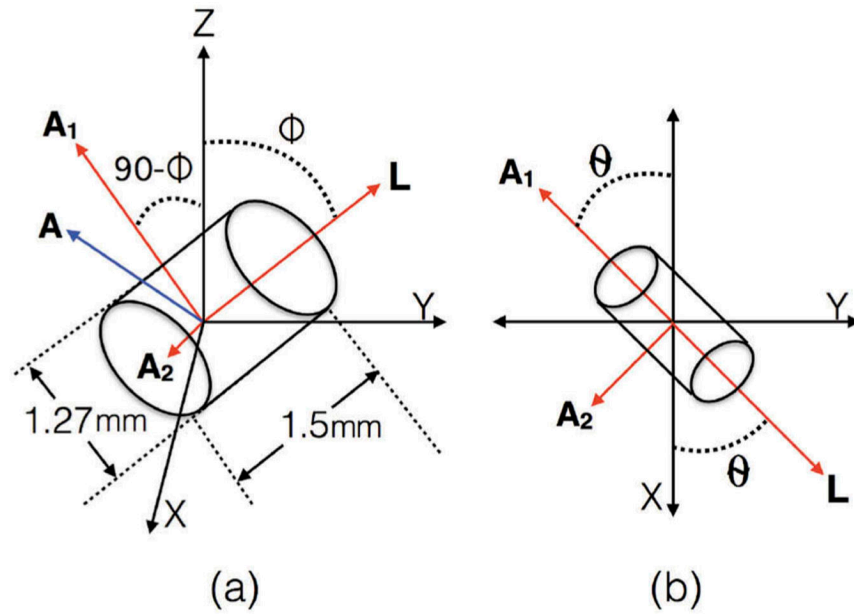


Figure 3.

The reference frames characterising DBS electrode orientation: (a) The inclined cylinder represents a DBS lead contact in two reference frames, $\mathbf{B} = \{\mathbf{X}, \mathbf{Y}, \mathbf{Z}\}$ and $\mathbf{N} = \{\mathbf{L}, \mathbf{A}_1, \mathbf{A}_2\}$. The principal vectors of basis \mathbf{N} are specified in spherical coordinates with respect to basis \mathbf{B} . For example, the elevation of the longitudinal axis \mathbf{L} is denoted by θ . The polar axis \mathbf{A}_1 , inscribes $90 - \phi$ degrees with the positive \mathbf{Z} axis. The polar axis \mathbf{A}_2 is along the cross product of vectors \mathbf{L} and \mathbf{A}_1 . \mathbf{A} is a linear combination of vectors \mathbf{A}_1 and \mathbf{A}_2 . (b) The azimuth of \mathbf{L} is θ and is depicted in the top view of the contact orientation shown in subfigure a. \mathbf{A}_2 is perpendicular to a plane containing \mathbf{L} , \mathbf{A}_1 , and the positive \mathbf{Z} axis.

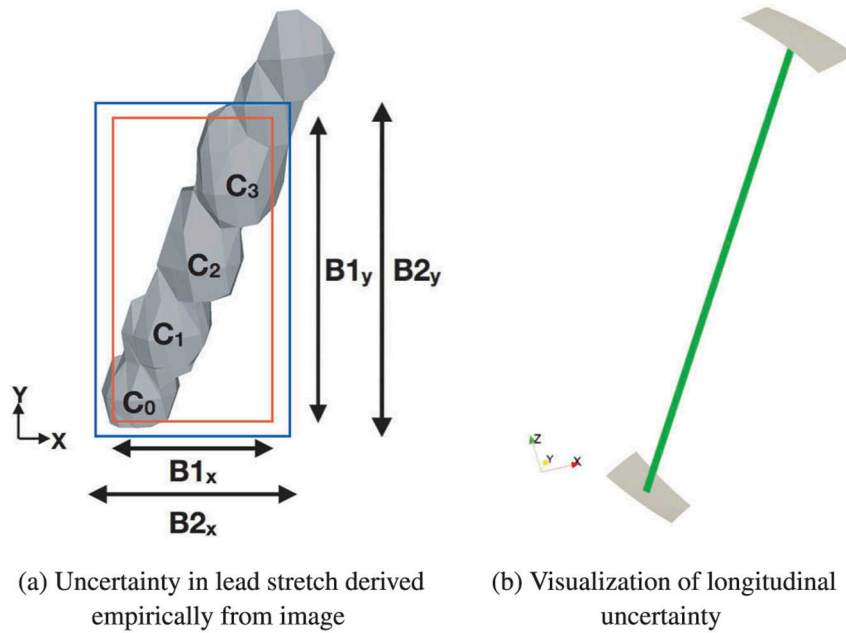


Figure 5.

The quantification of longitudinal uncertainty: (a) An isosurface is reconstructed from a synthetic dataset. The approximate spread of the four contacts along the X and Y directions is visually determined for the isosurface. The red and blue boxes denote imaging planes of an underlying synthetic volume that represent uncertainty in the physical boundaries of the four contacts [c_0 , c_1 , c_2 , c_3]. (b) The longitudinal uncertainty is quantified by matching the bounds derived from the isosurface, as shown in subfigure (a), and the bounds computed analytically, as described in Section 3.1. Grey patches denote a solid angle representing directional uncertainty, and a green line represents the true trajectory for the synthetic dataset.

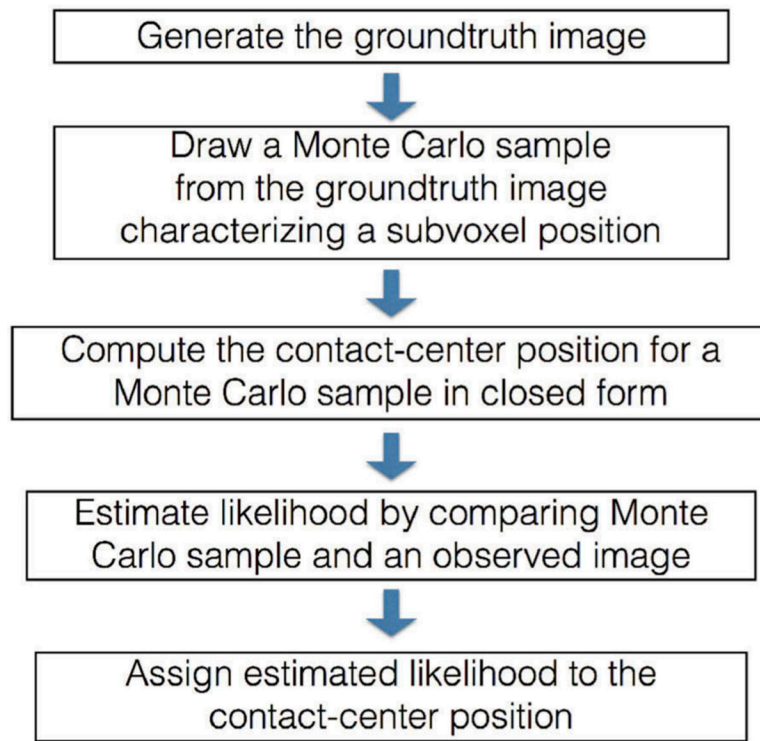


Figure 6. A schematic depicting a method for estimating uncertainty in contact-centre positions at subvoxel levels.

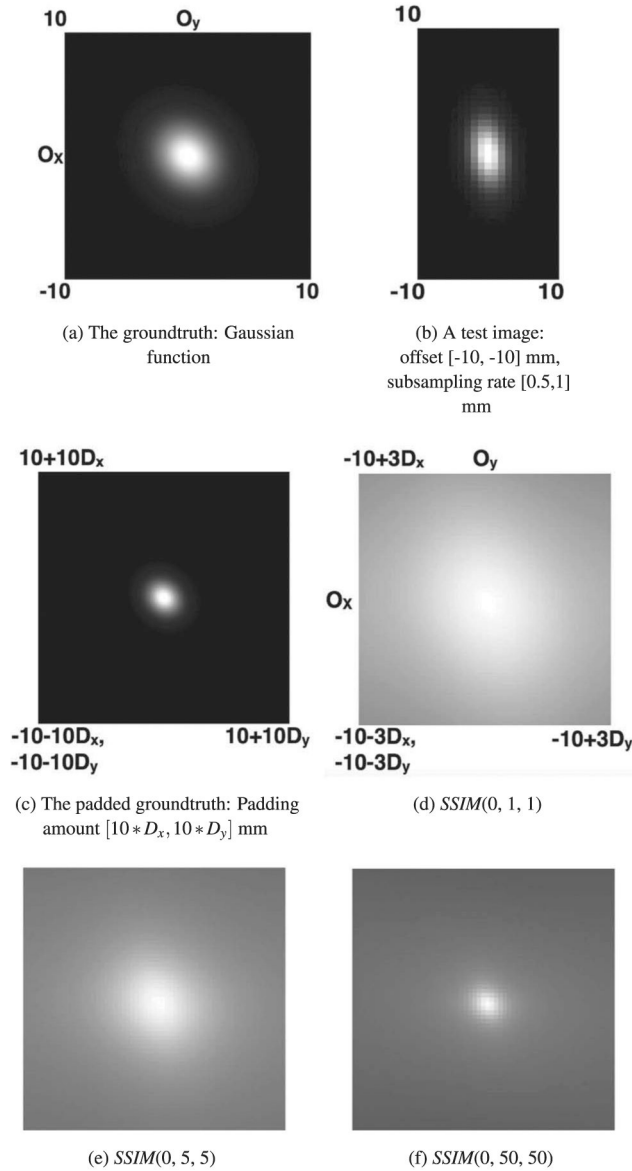


Figure 7.

The visualisation of uncertainty at subvoxel positions for a 2D synthetic image: (a) A Gaussian function with the mean $[0,0]$ mm, the variance 5mm^2 , and the covariance 0.3mm^2 . (b) A test image is generated by starting at the offset position $[O_x, O_y] = [-10, -10]$ mm in the groundtruth image and a subsampling rate $[D_x, D_y] = [0.5, 1]$ mm. (c) The groundtruth image is padded with $[10 * D_x, 10 * D_y]$ mm on both sides along the **X** and **Y** directions. Monte Carlo samples are drawn from the padded image by sampling offsets in the range $[-10 - 3 * D_x, -10 + 3 * D_x]$ mm and $[-10 - 3 * D_y, -10 + 3 * D_y]$ mm along the **X** and **Y** directions, respectively, at the intervals of $[0.1, 0.1]$ mm. For each sample, the subsampling rate is $[D_x, D_y] = [0.5, 1]$ mm. All samples in the specified offset ranges are compared with the test image using the **SSIM** index. The subfigures (d), (e) and (f) visualise a grey map of **SSIM** index values. The true value of the offset for the test image, i.e. $[-10, -10]$ mm, is

recovered sufficiently well in all three cases. The first, second, and last parameters of the **SSIM** index indicate intensity, contrast, and structural similarity weights, respectively.

Author Manuscript

Author Manuscript

Author Manuscript

Author Manuscript

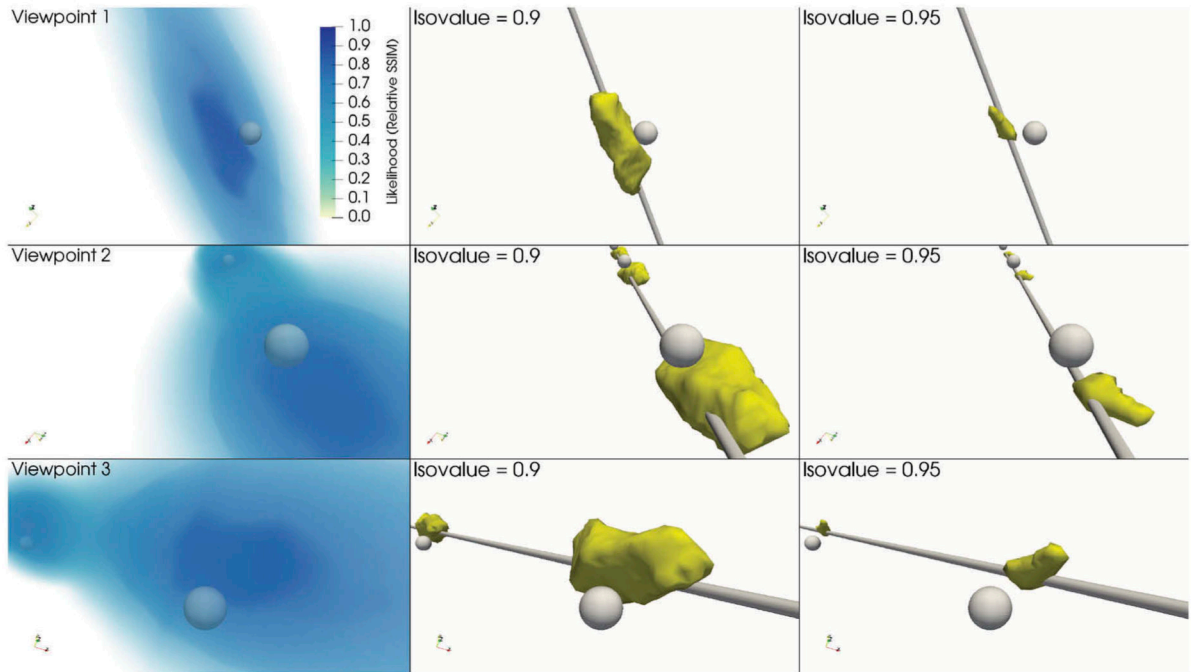


Figure 8.

The visualisation of positional uncertainties at subvoxel levels for the synthetic dataset: The left column shows the volume rendering of relative likelihood values for contact-centre positions. The middle and the right columns visualise isosurfaces for relative likelihood values 0.9 and 0.95, respectively. Each row corresponds to a fixed viewpoint and zoom-in level. Relative likelihood values are estimated for contact centres c along the mean of uncertain trajectories estimated in Section 3.2.2. In the middle and right columns, the mean trajectory is depicted by a solid grey line. The spherical glyphs depict the true contact-centre positions for the test dataset. In the left column, volume visualisations represent the positional distribution of contact centres in which each voxel is assigned the relative likelihood value computed using the **SSIM** index. In the transfer function for volume rendering, higher opacity is mapped to higher likelihood ranges and vice versa. The empirically computed standard deviations from the mean contact-centre positions for isosurfaces with relative likelihood values of 0.9 and 0.95 are 0.38 mm and 0.28 mm, respectively. The interactivity of the visualisation enables us to explore the overall shape of the likelihood volume as well as the positions of true contact centres with respect to the likelihood volume.

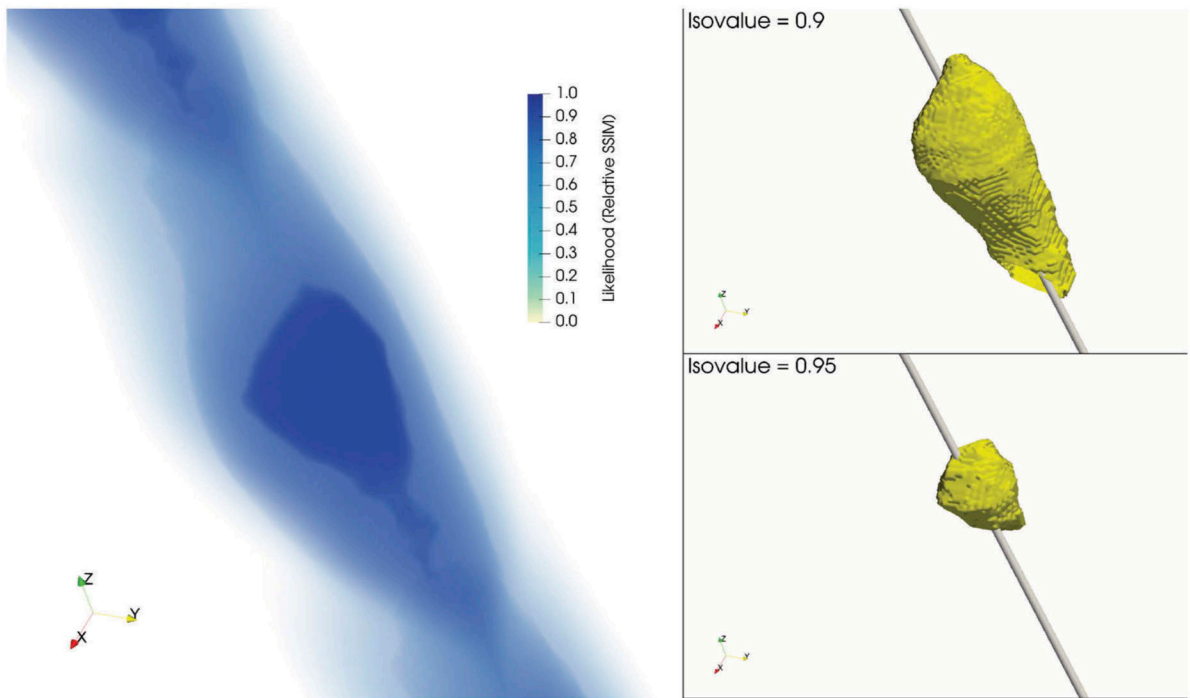


Figure 9.

The visualisation of positional uncertainties at subvoxel levels for the real dataset: The left column shows volume visualisation and the right column shows isosurface visualisations of spatial distributions estimated for contact centres c along the mean of uncertain trajectories estimated in Section 3.2.2. In the right column, the mean trajectory is represented by a grey line. In the left image, the volume visualisation represents the positional distribution of contact centres, where each voxel in the volume represents the relative likelihood value computed using the **SSIM** index. In the transfer function for volume rendering, higher opacity is mapped to higher likelihood ranges and vice versa. The top right image shows an isosurface containing contact centres with a relative likelihood of 0.9 or higher. The bottom right image shows a similar visualisation for the relative likelihood of 0.95. The empirically computed standard deviations from the mean contact-centre positions for isosurfaces with relative likelihood values of 0.9 and 0.95 are 0.71 mm and 0.48 mm, respectively.

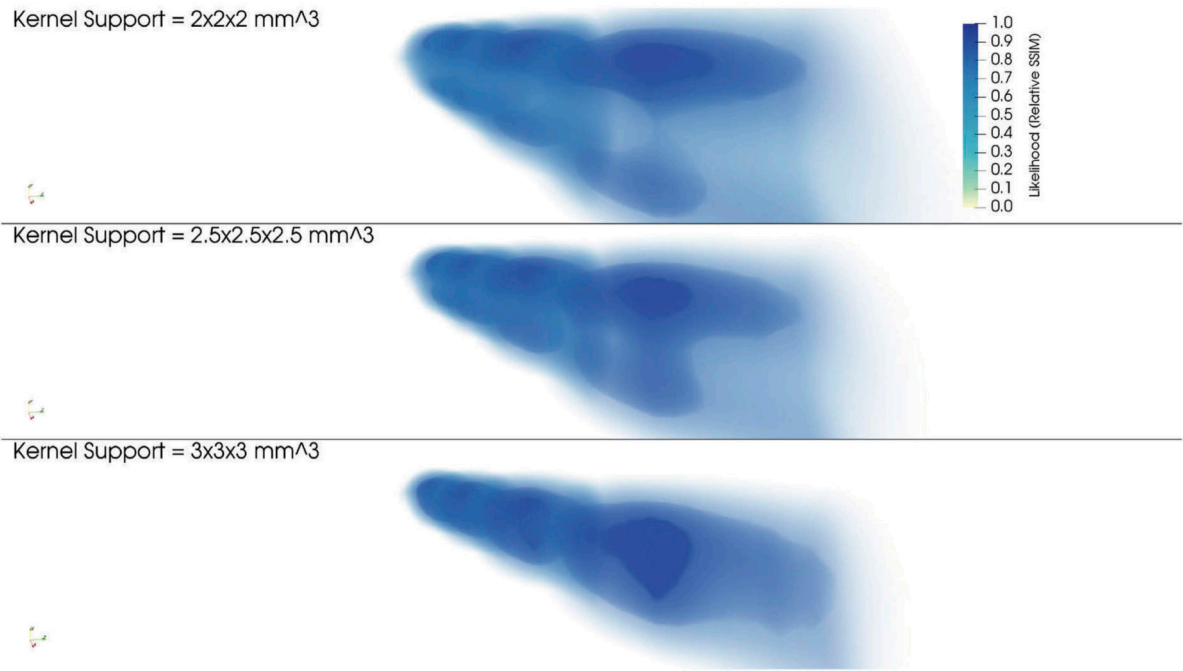


Figure 10.

The sensitivity of positional uncertainty quantification to the choice of kernel width: All images visualise positional uncertainties in contact centres for the real dataset and are rendered with the same transfer function. The distribution is discontinuous, giving rise to the visualisation artefacts when the choice of kernel width is relatively low. As the kernel width is increased from $2 \times 2 \times 2 \text{ mm}^3$ to $3 \times 3 \times 3 \text{ mm}^3$, the probability density visualisations for contact-centre positions get smoother and more compact. The visualisations can assist in gaining insight into the parameter values associated with kernels for simulating CT-specific partial volume effects. The regions of relatively high positional probabilities, however, are consistently recovered for all kernel widths.